

# Probing Many-Body Interactions in Monolayer Transition-Metal Dichalcogenides

Benedikt Scharf,<sup>1,\*</sup> Zefang Wang,<sup>2,†</sup> Dinh Van Tuan,<sup>3</sup> Jie Shan,<sup>2</sup> Kin Fai Mak,<sup>2</sup> Igor Žutić,<sup>1</sup> and Hanan Dery<sup>3,4,‡</sup>

<sup>1</sup>*Department of Physics, University at Buffalo, State University of New York, Buffalo, NY 14260, USA*

<sup>2</sup>*Department of Physics and Center for Two-Dimensional and Layered Materials, The Pennsylvania State University, University Park, Pennsylvania 16802-6300, USA*

<sup>3</sup>*Department of Electrical and Computer Engineering, University of Rochester, Rochester, New York 14627, USA*

<sup>4</sup>*Department of Physics and Astronomy, University of Rochester, Rochester, New York 14627, USA*

(Dated: June 24, 2016)

Many-body interactions in monolayer transition-metal dichalcogenides are strongly affected by their unique band structure. We study these interactions by measuring the energy shift of neutral excitons (bound electron-hole pairs) in gated WSe<sub>2</sub> and MoSe<sub>2</sub>. The gate-induced charge density screens the electron-hole Coulomb attraction and renormalizes the bandgap energy via exchange and correlation interactions. We compute the energy shift of neutral excitons as a function of charge density with the Bethe-Salpeter equation. The random-phase approximation gives a good experimental agreement, and we find that both disorder and temperature suppress screening. The disorder localizes the gate-induced charge, while increasing the temperature excites the free charge. Screening of the Coulomb attraction between the photoexcited electron-hole pairs is less effective in both cases. We resolve the contributions of the bandgap renormalization and screened potential by comparing the results of WSe<sub>2</sub> and MoSe<sub>2</sub>, due to their distinct spin-split conduction bands.

Monolayer transition-metal dichalcogenides (ML-TMDs) offer unique opportunities to test the manifestations of many-body interactions through changes in the charge density [1–10]. Their two-dimensional (2D) character and reduced screening enable the formation of tightly bound excitons [11–32], whose response to gate voltage provides valuable information on the underlying many-body interactions. Focusing on the energy position of the neutral exciton,  $X^0$ , the gate-induced charge density has two competing effects. The first one is a redshift due to the shrinkage of the bandgap, caused by exchange and correlation [33–35]. The second effect is a blueshift due to reduced binding energy, caused by screening of the Coulomb attraction between the photoexcited electron-hole pairs [33–35]. These effects are best seen in ML-TMDs, in which a large  $X^0$  binding energy allows us to probe many-body interactions in a wide range of charge density and temperature [24, 36].

In this Letter, we experimentally quantify the blueshift of excitons in gated ML-TMDs structures by optical reflectance spectroscopy and theoretically explain the measured blueshift using a transparent model in which the many-body interactions appear as parameters in the Bethe-Salpeter equation (BSE) of  $X^0$ . Our key findings are: (i) The use of the Thomas-Fermi approximation (TFA) for screening is inadequate and largely overestimates the blueshift. A much better agreement with experiment is achieved within the random-phase approximation (RPA) for screening. As commonly done in semiconductors, the use of the statically screened potential is sufficient to explain the absorption spectrum of  $X^0$  [33, 37]. (ii) Including disorder is crucial to explain the measured blueshift due to pronounced contributions from adatoms and substrate imperfections in materials with large surface to volume ratio. These imperfections

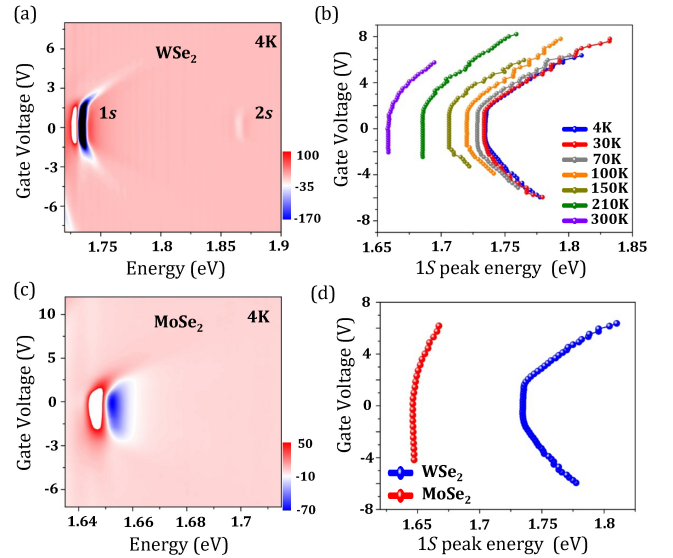


FIG. 1. Measured blueshift of  $X^0$  in gated ML-TMDs. (a) and (c) Colormaps of the derivative of the reflectance contrast spectra at 4K under varying gate voltages in ML-WSe<sub>2</sub> and ML-MoSe<sub>2</sub>. (b) Energy of the ground-state  $X^0$  (1s) as a function of gate voltage at various temperatures in ML-WSe<sub>2</sub>. (d) Comparison of the 1s peak energy as a function of gate voltage in ML-WSe<sub>2</sub> and MoSe<sub>2</sub> at 4K.

localize the gate-induced charge at small voltages [38], thereby suppressing the screening at low densities. (iii) The absorption of  $X^0$  is not suppressed at elevated  $T$  due to the diminished effectiveness of thermally excited charge to screen the electron-hole attraction. As a result, the integrated absorption intensity of the  $X^0$  peak does not decay with  $T$ . (iv) A comparison of the energy shift in tungsten (W)- and molybdenum (Mo)-based compounds

allows us to decouple the contributions from bandgap renormalization and screened electron-hole interaction. This decoupling is manifested by the unique order of the spin-split conduction bands in the time-reversed  $K$  and  $K'$  points of the Brillouin zone [24, 40–42].

Figure 1 shows the measured reflectance contrast spectra in the energy range of  $X^0$  in gated ML-WSe<sub>2</sub> and ML-MoSe<sub>2</sub>. The MLs were embedded in thin hexagonal boron-nitride (h-BN) layers, which also serve as the top and back gate dielectric in the dual gate field-effect transistors with few-layer graphene as both gate electrodes. These vertical heterostructures were fabricated by dry transfer of constituent atomically thin layers of materials that were obtained by mechanical exfoliation of bulk crystals [43]. The reflectance contrast was measured by comparing the reflectivity from areas of the heterostructures with and without the ML [23]. To increase the contrast for the resonance features, the derivative of the reflectance contrast is shown in Fig. 1(a) and (c). Combinations of the top and back gates were applied to vary the doping density while keeping a zero vertical electric field across the ML-TMDs. The doping density can be estimated from the combined gate voltage using the top and bottom gate capacitances,  $1\text{ V} \sim 7.5 \times 10^{11}\text{ cm}^{-2}$ , for the two devices shown [44]. The measurements clearly show that  $X^0$  blueshifts for both electron and hole doping (positive and negative gate voltage), and that the effect persists up to room temperature. The shift is stronger for electron doping than for hole doping, and it is significantly larger in ML-WSe<sub>2</sub> than in ML-MoSe<sub>2</sub>. We also note that no shift is observed for small doping densities.

To model the observed behavior of  $X^0$ , we consider excitations at the  $K$  and  $K'$  points from the topmost spin-split valence band into the lowest conduction band [24]. We assume parabolic bands  $\epsilon_{v\mathbf{k}} = -\hbar^2 k^2/2m_v$  and  $\epsilon_{c\mathbf{k}} = E_g + \hbar^2 k^2/2m_c$ , where  $E_g$  is the bandgap,  $m_{c(v)}$  is the electron (hole) effective mass, and  $\mathbf{k}$  is the crystal momentum measured with respect to  $K/K'$ . This simple model offers very efficient computation of the binding energy, and yet it provides a good experimental agreement. We use the BSE to calculate the exciton binding energy,  $\Omega_S$ , where  $S$  denotes the discrete level, and its wave function in reciprocal space,  $\mathcal{A}_{\mathbf{k}}^S$  [34, 35, 46],

$$\sum_{\mathbf{k}'} \mathcal{H}_{\mathbf{k},\mathbf{k}'} \mathcal{A}_{\mathbf{k}'}^S = \Omega_S \mathcal{A}_{\mathbf{k}}^S, \quad (1)$$

$$\mathcal{H}_{\mathbf{k},\mathbf{k}'} = (\epsilon_{\mathbf{k}} + \Sigma_{\text{eh}}) \delta_{\mathbf{k},\mathbf{k}'} - \frac{\sqrt{|F(\mathbf{k})|} W(\mathbf{k} - \mathbf{k}') \sqrt{|F(\mathbf{k}')|}}{A}.$$

$A$  is the 2D unit area,  $\epsilon_{\mathbf{k}} = \epsilon_{c\mathbf{k}} - \epsilon_{v\mathbf{k}}$ , and  $F(\mathbf{k}) = f(\epsilon_{v\mathbf{k}}) - f(\epsilon_{c\mathbf{k}})$  with the Fermi-Dirac distribution  $f(\epsilon)$  [47]. The dependence on the free-charge density is governed by the screening of the electron-hole interaction,  $W(\mathbf{k} - \mathbf{k}')$ , and by the bandgap renormalization  $\Sigma_{\text{eh}}$ . Since optical transitions involve similar-spin energy bands, a key difference between Mo- and W-based compounds is that optical transitions in ML-MoX<sub>2</sub> (ML-WX<sub>2</sub>) involve the lower

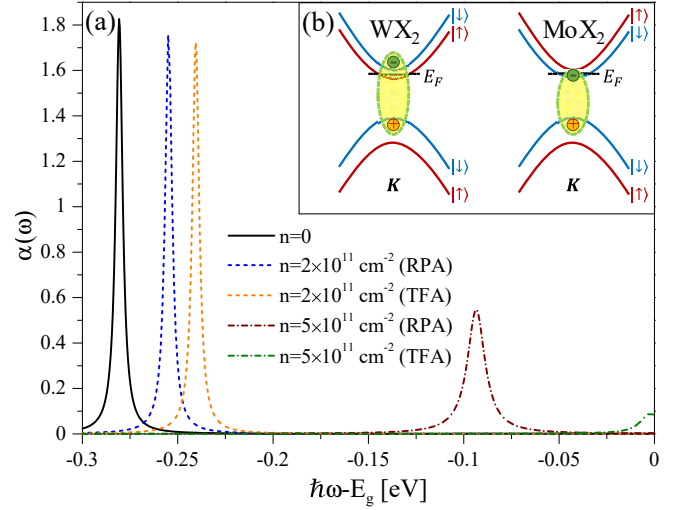


FIG. 2. (a) Absorption profile of the ground-state  $X^0$  in ML-WSe<sub>2</sub> embedded in h-BN for different  $n$ -dopings as calculated from the static RPA or the TFA. Here,  $m_v = 0.36m_0$ ,  $m_c = 0.29m_0$  (and  $m_c = 0.4m_0$  for the lower conduction band),  $\epsilon = 2.7$ ,  $r_0 = 3.1\text{ nm}$ ,  $T = 5\text{ K}$ , and  $s = 5\text{ meV}$ . (b) Schematic optical transitions of the lowest energy  $X^0$  in W-based (left) and Mo-based (right) MLs. The gate-induced charge is populated in the lower spin-split valleys.

(upper) spin-split valleys of the conduction band [40, 42], as shown in Fig. 2(b). We first describe the dependence of the free-charge density,  $n_f$ , on disorder and then formulate the dependence of  $W(\mathbf{k} - \mathbf{k}')$  and  $\Sigma_{\text{eh}}$  on  $n_f$ .

The large surface to volume ratio in ML-TMDs renders their transport and optical properties highly susceptible to charged impurity disorder from adatoms and substrate imperfections [38]. We use a Gaussian distribution to parametrize the potential fluctuations. This simple model is appealing due to its success in explaining transport properties in graphene [48], and the fact that it supports the observed inhomogeneous broadening of  $X^0$  in TMDs [49]. Relevant to our study is the change in the density of states (DOS) [38],

$$D(\epsilon) = \frac{D_0}{2} \text{erfc}\left(\frac{-\epsilon}{\sqrt{2}s}\right), \quad D_0 = \frac{g_s g_v m_{c(v)}}{2\pi \hbar^2}, \quad (2)$$

where  $s$  is the root-mean-square energy fluctuation of the disorder potential, while  $g_s = 1$  and  $g_v = 2$  are the spin and valley degeneracy, respectively. In the disorder-free case,  $s = 0$ , the DOS regains its ideal step-function form,  $D(\epsilon > 0) = D_0$ . For finite disorder,  $s \neq 0$ , we get a tail of localized states for negative energies. The total charge density is provided by the sum of free and disorder-induced localized charge densities,

$$n = n_f + n_\ell, \quad (3)$$

$$n_i = D_0 \int_{\epsilon_1}^{\epsilon_2} d\epsilon \left[ \frac{1}{2} \text{erfc}\left(\frac{-\epsilon}{\sqrt{2}s}\right) \right] \frac{1}{\exp[\beta(\epsilon - \bar{\mu})] + 1},$$

where  $\beta = 1/k_B T$  and  $\tilde{\mu}$  is an effective chemical potential [39]. The integration is between 0 and  $\infty$  for the free charge density ( $i = f$ ), and between  $-\infty$  and 0 for the localized one ( $i = \ell$ ).

Screening of  $X^0$  and the bandgap renormalization effects are mediated by the free-charge carriers since they can move next to the  $X^0$  and next to each other. Our focus on  $X^0$  allows us to employ static screening for modeling the interaction in (1) [35],

$$W(\mathbf{q}) = \frac{v_{\mathbf{q}}}{1 + v_{\mathbf{q}}\Pi(q, T)}, \quad v_{\mathbf{q}} = \frac{2\pi e^2}{\varepsilon q + r_0 q^2}, \quad (4)$$

where  $v_{\mathbf{q}}$  and  $\Pi(q, T)$  denote, respectively, the bare electrostatic potential and longitudinal polarization function. The former includes geometrical effects [44, 51, 52], where  $\varepsilon$  is the average dielectric constant from the bottom and top materials surrounding the ML, and  $r_0$  is the polarizability of a ML expressed in terms of its effective dielectric constant and thickness [44]. Below we use  $r_0 = 3.1$  nm (4.1 nm) to simulate ML-WSe<sub>2</sub> (ML-MoSe<sub>2</sub>), encapsulated by h-BN for which  $\varepsilon=2.7$  [44, 53].

The dependence of the screened electron-hole interaction,  $W(\mathbf{q})$ , on the free-charge density is governed by the longitudinal polarization function. In the TFA, the  $T = 0$  polarization function of an ideal 2D system is simply given by its DOS [50],

$$\Pi_{\text{TF}}(q, T = 0) = D_0, \quad v_{\mathbf{q}}\Pi_{\text{TF}}(q, 0) = \frac{\kappa_0}{q + r_0 q^2/\varepsilon}, \quad (5)$$

where  $\kappa_0 = g_s g_v / a_B$  is the screening wavenumber expressed in terms of the effective Bohr radius of the electron (hole),  $a_B = \hbar^2 \varepsilon / e^2 m_{c(v)}$ . The TFA is oversimplified since it strongly overestimates the screening, leading to unphysical results where the screening has a similar effect for large and small values of  $n_f$  (the TF screening parameter,  $\kappa_0$ , is independent of  $n_f$  when  $T \rightarrow 0$  in an ideal 2D electron gas). To resolve this problem, we invoke the RPA with the  $T = 0$  static polarization function [50]

$$\Pi(q, 0) = D_0 \left[ 1 - \sqrt{1 - (2k_F/q)^2} \Theta(q - 2k_F) \right]. \quad (6)$$

Here,  $\Theta(x)$  is a step function and  $k_F = \sqrt{4\pi n_f / g_s g_v}$  is the zero-temperature Fermi wavenumber. This polarization function guarantees that the screening is not constant, but decays for  $q > 2k_F \propto \sqrt{n_f}$ . The  $T$ -dependent static polarization function is calculated by [54],

$$\Pi(q, T) = \frac{\beta}{4} \int_0^\infty d\epsilon_F \frac{\Pi(q, 0)}{\cosh^2 [\beta (\mu - \epsilon_F) / 2]}, \quad (7)$$

where  $\epsilon_F = \hbar^2 k_F^2 / 2m_{c(v)}$  is the Fermi energy of the background electron (hole) density at  $T = 0$ , and  $\mu$  is the chemical potential determined by  $n_f(T)$ . The TFA is recovered at long-wavelengths ( $q \rightarrow 0$ ),

$$(q + r_0 q^2 / \varepsilon) v_{\mathbf{q}} \Pi(q, T) \rightarrow \kappa(T) = \kappa_0 [1 - \exp(-\beta \epsilon_F)]. \quad (8)$$

The main effect from an increase in  $T$  is an increase in the effective screening length.

The final component in the theory is the dependence of the bandgap renormalization on the free-charge density,  $\Sigma_{\text{eh}}(n_f)$ . To quantify this dependence, we use the plasmon-pole approximation to model the dynamics of the screened dielectric function [55–57]. The appeal of this simple approximation is in its capability to achieve qualitative agreement with experiment while keeping the calculation concise [33]. One can then separate the bandgap renormalized energy into contributions from exchange

$$\Sigma_{i,x}(\mathbf{k}) = - \int d^2 q v_{\mathbf{q}} f(\epsilon_{i,\mathbf{k}-\mathbf{q}}), \quad (9)$$

and correlation

$$\begin{aligned} \Sigma_{i,c}(\mathbf{k}) = & \int \frac{d^2 q}{(2\pi)^2} \int \frac{d(\hbar\omega)}{\pi} \frac{f(\epsilon_{i,\mathbf{k}-\mathbf{q}}) + g(-\hbar\omega)}{\epsilon_{i,\mathbf{k}} - \epsilon_{i,\mathbf{k}-\mathbf{q}} - \hbar\omega} v_{\mathbf{q}} \\ & \times \frac{\pi \omega_{\text{pl}}^2(q)}{2\omega_q} [\delta(\omega + \omega_q) - \delta(\omega - \omega_q)], \end{aligned} \quad (10)$$

where  $i = c$  ( $i = v$ ) if the background free charges are electrons (holes), and  $g(\epsilon)$  the Bose-Einstein distribution. The plasma frequency is  $\omega_{\text{pl}}(q) = \sqrt{2\pi e^2 n_f q / \varepsilon m_i}$ , and the pole energy  $\hbar\omega_q = \hbar\omega_{\text{pl}}(q) \sqrt{1 + q/\kappa(T)}$ . The exchange and correlation energies show a weak dependence on  $T$  and wavevector values for electrons inside the Fermi sea,  $\epsilon_{\mathbf{k}} \leq \epsilon_F$  [55]. We therefore assume the populated valleys to experience a rigid energy shift,  $\Sigma_{\text{eh},\mathbf{k}=0}$ , computed at the band edge and at  $T = 0$ .

Putting the pieces together, we solve Eq. (1) and use its eigenstates and eigenvalues to calculate the optical absorption

$$\alpha(\omega) = \frac{4e^2 \pi^2 g_s g_v |d_{\text{vc}}|^2}{c\omega} \frac{1}{A} \sum_S \left| \sum_{\mathbf{k}} \sqrt{|F(\mathbf{k})|} \mathcal{A}_{\mathbf{k}}^S \right|^2 \times \mathcal{L}(\hbar\omega; \Omega_S, \Gamma). \quad (11)$$

Here,  $\hbar\omega$  is the photon energy,  $c$  the light velocity, and  $d_{\text{vc}} = 5 \times 10^7$  cm/s is the single-particle dipole-matrix element for transition between the valence and conduction bands, considered wavevector-independent due to the smallness of the Fermi energy with the band gap [33]. The Lorentzian function,  $\mathcal{L}(\hbar\omega; \Omega_S, \Gamma)$ , accounts for homogenous broadening due to electron-electron and electron-lattice interactions [49, 58, 59].

Using ML-WSe<sub>2</sub> parameters [41] and  $s = 5$  meV, Fig. 2 (a) shows that the TFA (8) predicts a fast blueshift of the 1s peak with increasing density and no longer any pronounced excitonic effects at  $n = 5 \times 10^{11}$  cm<sup>-2</sup>. This behavior presents a marked contrast to the observed behavior in our experiment as well as in previous experimental works [2, 7]. Specifically, one finds that  $X^0$  can persist up to densities of the order of  $10^{12}$  cm<sup>-2</sup> in the

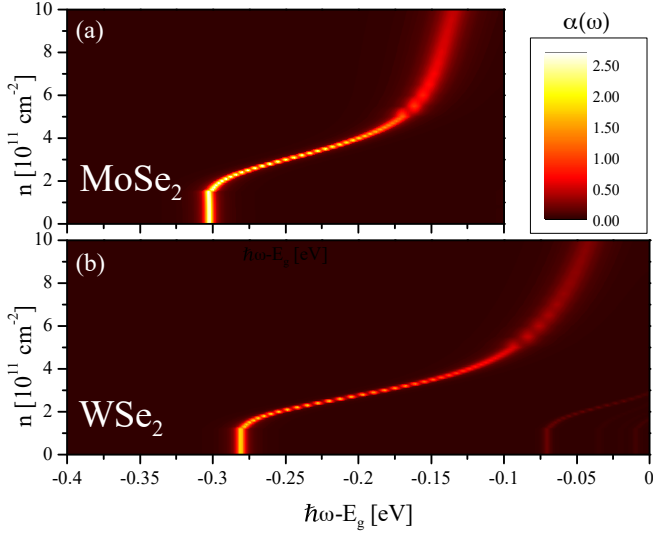


FIG. 3. Absorption of (a) ML-MoSe<sub>2</sub> and (b) ML-WSe<sub>2</sub> for different  $n$ -dopings as calculated with static RPA screening and the same parameters as in Fig. 2 and  $m_v = 0.6m_0$ ,  $m_c = 0.5m_0$ ,  $\varepsilon = 2.7$ , and  $r_0 = 4.1$  nm for ML-MoSe<sub>2</sub> [41].

experiment [44]. Therefore, we conclude that the screening in ML-TMDs is much better modeled by the RPA, while the TFA overestimates its effect.

Figure 3 compares the density dependence of the absorption of electron-doped ML-MoSe<sub>2</sub> and ML-WSe<sub>2</sub> calculated with static RPA screening. Including disorder is crucial to account for the fact that no energy shift is measured for small doping densities [see Figs. 1 (b) and (d)]. As the density increases, the 1s and 2s peaks blueshift faster for ML-WSe<sub>2</sub> than for ML-MoSe<sub>2</sub>. This qualitative difference between the two compounds is also corroborated by our experimental results, as shown in Fig. 1 (d). The difference originates from the fact that optical transitions involve the lower (upper) spin-split conduction band in ML-MoSe<sub>2</sub> (ML-WSe<sub>2</sub>). At low  $T$  and for free-electron densities smaller than  $\sim 10^{13}$  cm<sup>-2</sup>,  $\Sigma_{\text{eh}}$  is sizable in ML-MoX<sub>2</sub>, but negligible in ML-WX<sub>2</sub> since only the lower spin-split valleys are populated [60]. As a result, the blueshift due to reduced binding energy at elevated electron densities is counteracted by the energy redshift of the bandgap mostly in ML-MoSe<sub>2</sub>.

Finally, the  $T$ -dependence is modeled in Fig. 4. The lowered peak amplitude at elevated  $T$  originates from the introduction of  $T$ -dependent homogeneous broadening [44]. Nonetheless, the integrated amplitude increases with  $T$ . This counterintuitive behavior can be understood by the fact that thermally-excited electrons ‘cannot keep still’, and therefore are less effective in screening. The suppressed screening helps to keep the  $X^0$  bound at elevated  $T$ . This behavior is unique for materials with large binding energies; it cannot be observed if the binding energy is smaller or comparable to  $k_B T$  due to ionization of the  $X^0$  states.

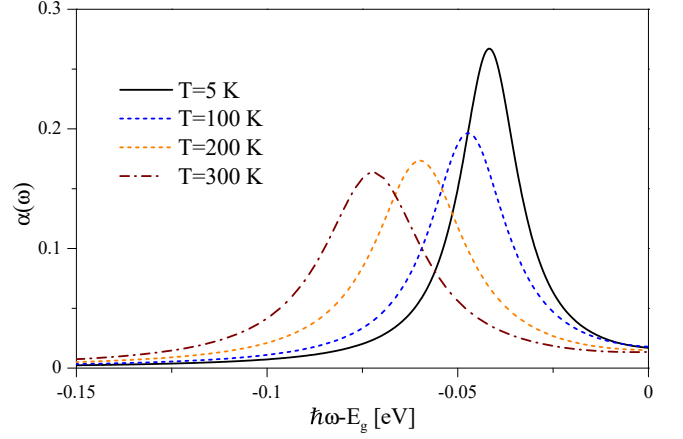


FIG. 4. Absorption profile of the ground-state  $X^0$  in ML-WSe<sub>2</sub> for  $n = 10^{12}$  cm<sup>-2</sup> at different  $T$ , as calculated with static RPA screening and the parameters from Fig. 2. For  $s = 5$  meV,  $n_\ell \approx 3.3 \times 10^{11}$  cm<sup>-2</sup> at each  $T$  shown.

In conclusion, we have measured the doping density dependence of the neutral-exciton energy shift in monolayer transition-metal dichalcogenides. By using a computationally inexpensive model, we solve the Bethe-Salpeter equation to qualitatively explain several many-body effects. In order to model the screening in these materials, it is crucial to go beyond the Thomas-Fermi model and use at least the static random-phase approximation. The bandgap renormalization was found to affect the position of the neutral exciton in molybdenum-based compounds, while being weak in tungsten-based compounds due to the difference in the ordering of their spin-split conduction bands. Disorder and finite-temperature effects were included in the model, providing ways to suppress the screening effect. While disorder was introduced phenomenologically, the model is still able to quantitatively capture the main features of the experiment. However, future developments are needed to better understand the role of disorder. For example, modeling of the blueshift may improve quantitatively by measuring the disorder parameters and characterizing its behavior, as well as by treating disorder self-consistently within the random-phase approximation. Ultimately, the strong exciton optical transitions in these materials will find use in a variety of optoelectronic applications [21, 24, 32, 61–63], offering a wide range of wavelength tuning controlled by a gate voltage in van der Waals heterostructures.

The work at the University at Buffalo was supported by U.S. DOE, Office of Science BES, under Award DESC0004890 (I.Ž.), by U.S. ONR N000141310754 (B.S.), and the German Science Foundation (DFG) Grant No. SCHA 1899/1-1 (B.S.). The work at the University at the Pennsylvania State University was supported by the Department of Energy under Contract No. DESC0013883 (spectroscopy measurements), DESC0012635 (sample and device fabrication), and the

National Science Foundation under Contract No. DMR-1410407 (Z.W). The work at the University of Rochester was supported by the Department of Energy under Contract No. DE-SC0014349, National Science Foundation under Contract No. DMR-1503601, and the Defense Threat Reduction Agency under Contract No. HDTRA1-13-1-0013.

\* benedikt.scharf@ur.de

† Zefang Wang and Benedikt Scharf have contributed equally to this work.

‡ hanan.dery@rochester.edu

- [1] J. T. Ye, Y. J. Zhang, R. Akashi, M. S. Bahramy, R. Arita, Y. Iwasa, *Science* **338**, 1193 (2012).
- [2] K. F. Mak, K. He, C. Lee, G. H. Lee, J. Hone, T. F. Heinz, and J. Shan, *Nat. Mater.* **12**, 207 (2013).
- [3] A. M. Jones, H. Yu, N. J. Ghimire, S. Wu, G. Aivazian, J. S. Ross, B. Zhao, J. Yan, D. G. Mandrus, D. Xiao, W. Yao, and X. Xu, *Nat. Nano.* **8**, 634 (2013).
- [4] J. S. Ross, S. Wu, H. Yu, N. J. Ghimire, A. M. Jones, G. Aivazian, J. Yan, D. G. Mandrus, D. Xiao, W. Yao, X. Xu, *Nat. Commun.* **4**, 1474 (2013).
- [5] M. M. Ugeda, A. J. Bradley, S.-F. Shi, F. H. da Jornada, Y. Zhang, D. Y. Qiu, W. Ruan, S.-K. Mo, Z. Hussain, Z.-X. Shen, F. Wang, S. G. Louie, and M. F. Crommie, *Nat. Mater.* **13**, 1091 (2014).
- [6] B. Ganchev, N. Drummond, I. Aleiner, and V. Falko, *Phys. Rev. Lett.* **114**, 107401 (2015).
- [7] A. Chernikov, A. M. van der Zande, H. M. Hill, A.F. Rigosi, A. Velauthapillai, J. Hone, and T. F. Heinz, *Phys. Rev. Lett.* **115**, 126802 (2015).
- [8] G. Plechinger, P. Nagler, J. Kraus, N. Paradiso, C. Strunk, C. Schüller, and T. Korn, *Phys. Status Solidi RRL* **9**, 457 (2015).
- [9] J. Shang, X. Shen, C. Cong, N. Peimyoo, B. Cao, M. Eginligil, and T. Yu, *ACS Nano* **9**, 647 (2015).
- [10] A. M. Jones, H. Yu, J. R. Schaibley, J. Yan, D. G. Mandrus, T. Taniguchi, K. Watanabe, H. Dery, W. Yao, and X. Xu, *Nat. Phys.* **12**, 323 (2016).
- [11] K. F. Mak, C. Lee, J. Hone, J. Shan, and T. F. Heinz, *Phys. Rev. Lett.* **105**, 136805 (2010).
- [12] A. Splendiani, L. Sun, Y. Zhang, T. Li, J. Kim, C.-Y. Chim, G. Galli, and F. Wang, *Nano Lett.* **10**, 1271 (2010).
- [13] T. Korn, S. Heydrich, M. Hirmer, J. Schmutzler, and C. Schüller, *Appl. Phys. Lett.* **99**, 102109 (2011).
- [14] Q. H. Wang, K. Kalantar-Zadeh, A. Kis, J. N. Coleman, M. S. Strano, *Nat. Nanotechnol.* **7**, 699 (2012).
- [15] T. Cheiwchanchamnangij and W. R. L. Lambrecht, *Phys. Rev. B* **85**, 205302 (2012).
- [16] A. Ramasubramaniam, *Phys. Rev. B* **86**, 115409 (2012).
- [17] H.-P. Komsa and A. V. Krasheninnikov, *Phys. Rev. B* **86**, 241201(R) (2012).
- [18] D. Xiao, G.-B. Liu, W. Feng, X. Xu, and W. Yao, *Phys. Rev. Lett.* **108**, 196802 (2012).
- [19] T. C. Berkelbach, M. S. Hybertsen, and D. R. Reichman, *Phys. Rev. B* **88**, 045318 (2013); *ibid.* **92**, 085413 (2015).
- [20] D. Y. Qiu, F. H. da Jornada, and S. G. Louie, *Phys. Rev. Lett.* **111**, 216805 (2013).
- [21] L. Britnell, R. M. Ribeiro, A. Eckmann, R. Jalil, B. D. Belle, A. Mishchenko, Y.-J. Kim, R. V. Gorbachev, T. Georgiou, S. V. Morozov, A. N. Grigorenko, A. K. Geim, C. Casiraghi, A. H. Castro Neto, and K. S. Novoselov, *Science* **340**, 1311 (2013).
- [22] Y. Song and H. Dery, *Phys. Rev. Lett.* **111**, 026601 (2013).
- [23] K. He, N. Kumar, L. Zhao, Z. Wang, K. F. Mak, H. Zhao, and J. Shan, *Phys. Rev. Lett.* **113**, 026803 (2014).
- [24] X. Xu, W. Yao, D. Xiao, and T. F. Heinz, *Nat. Phys.* **10**, 343 (2014).
- [25] A. Chernikov, T. C. Berkelbach, H. M. Hill, A. Rigosi, Y. Li, O. B. Aslan, D. R. Reichman, M. S. Hybertsen, and T. F. Heinz, *Phys. Rev. Lett.* **113**, 076802 (2014).
- [26] C. Zhang, H. Wang, W. Chan, C. Manolatu, and F. Rana, *Phys. Rev. B* **89**, 205436 (2014).
- [27] F. Wu, F. Qu, and A. H. MacDonald, *Phys. Rev. B* **91**, 075310 (2015).
- [28] P. Li and I. Appelbaum, *Phys. Rev. B* **92**, 195129 (2015).
- [29] D. K. Zhang, D. W. Kidd, K. Varga, *Nano Lett.* **15**, 7002 (2015).
- [30] C. Robert, D. Lagarde, F. Cadiz, G. Wang, B. Lassagne, T. Amand, A. Balocchi, P. Renucci, S. Tongay, B. Urbaszek, and X. Marie, *Phys. Rev. B* **93**, 205423 (2016).
- [31] A. V. Stier, K. M. McCreary, B. T. Jonker, J. Kono, S. A. Crooker, *J. Vac. Sci. Technol. B* **34**, 04J102 (2016).
- [32] K. F. Mak and J. Shan, *Nat. Photon.* **10**, 216 (2016).
- [33] H. Haug and S. W. Koch, *Quantum Theory of the Optical and Electronic Properties of Semiconductors*, 3rd ed. (World Scientific, Singapore, 1994).
- [34] H. Haug and S. Schmitt-Rink, *Prog. Quant. Electr.* **9**, 3 (1984).
- [35] S. Schmitt-Rink, C. Ell, and H. Haug, *Phys. Rev. B* **33**, 1183 (1986).
- [36] A. T. Hanbicki, K. M. McCreary, G. Kioseoglou, M. Currie, C. S. Hellberg, A. L. Friedman, and B. T. Jonker, *AIP Advances* **6**, 055804 (2016).
- [37] J. P. Löwenau, S. Schmitt-Rink, and H. Haug, *Phys. Rev. Lett.* **49**, 1511 (1982).
- [38] S. Das Sarma, E. H. Hwang, and Q. Li, *Phys. Rev. B* **88**, 155310 (2013).
- [39] Here,  $\tilde{\mu}$  is determined from the total density  $n$  via Eq. (3) and is only used to compute the free and localized densities. The free density  $n_f$  is then used to compute the Fermi energy  $\epsilon_F$  and chemical potential  $\mu = k_B T \ln [e^{\epsilon_F/k_B T} - 1]$  used throughout this work [38].
- [40] A. Kormányos, V. Zolyomi, N. D. Drummond, and G. Burkard, *Phys. Rev. X* **4**, 011034 (2014).
- [41] A. Kormányos, G. Burkard, M. Gmitra, J. Fabian, V. Zolyomi, N. D. Drummond, V. Fal'ko, *2D Mater.* **2**, 022001 (2015).
- [42] H. Dery and Y. Song, *Phys. Rev. B* **92**, 125431 (2015).
- [43] L. Wang, I. Meric, P. Y. Huang, Q. Gao, Y. Gao, H. Tran, T. Taniguchi, K. Watanabe, L. M. Campos, D. A. Muller, J. Guo, P. Kim, J. Hone, K. L. Shepard, and C. R. Dean, *Science* **342**, 614 (2013).
- [44] See Supplemental Material at the end of this document for more details. This information includes Ref. [45]
- [45] S. W. Koch, M. Kira, G. Khitrova, and H. M. Gibbs, *Nat. Mater.* **5**, 523 (2006).
- [46] M. Rohlfing, and S. G. Louie, *Phys. Rev. B* **62**, 4927 (2000).
- [47] Equation (1), as well as Eq. (11), is valid either for com-



- pletely occupied valence bands (and  $n$ -doping) or completely unoccupied conduction bands (and  $p$ -doping).
- [48] Q. Li, E. H. Hwang, and S. Das Sarma, *Phys. Rev. B* **84**, 115442 (2011).
  - [49] G. Moody, C. K. Dass, K. Hao, C.-H. Chen, L.-J. Li, A. Singh, K. Tran, G. Clark, X. Xu, G. Berghauser, E. Malic, A. Knorr, and X. Li, *Nat. Commun.* **6**, 8315 (2015).
  - [50] T. Ando, A. B. Fowler, and F. Stern, *Rev. Mod. Phys.* **54**, 437 (1982).
  - [51] L. V. Keldysh, *JETP Lett.* **29**, 658 (1979).
  - [52] P. Cudazzo, I. V. Tokatly, and A. Rubio, *Phys. Rev. B* **84**, 085406 (2011).
  - [53] B. Hunt, J. D. Sanchez-Yamagishi, A. F. Young, M. Yankowitz, B. J. LeRoy, K. Watanabe, T. Taniguchi, P. Moon, M. Koshino, P. Jarillo-Herrero, R. C. Ashoori, *Science* **340**, 1427 (2013).
  - [54] P. F. Maldague, *Surf. Sci.* **73**, 296 (1978).
  - [55] A. W. Overhauser, *Phys. Rev. B* **3**, 1888 (1971).
  - [56] T. M. Rice, *Nuovo Cimento* **23B**, 226 (1974).
  - [57] R. Zimmermann and M. Rösler, *Phys. Stat. Solidi B* **75**, 633 (1976).
  - [58] D. Huang, H. Y. Chu, Y. C. Chang, R. Houdre, and H. Morkoc, *Phys. Rev. B* **38**, 1246 (1988).
  - [59] A. Honold, L. Schultheis, J. Kuhl, and C. W. Tu, *Phys. Rev. B* **40**, 6442(R) (1989).
  - [60] H. Dery, arXiv:1604.00068.
  - [61] J. Lee, S. Bearden, E. Wasner, and I. Žutić, *Appl. Phys. Lett.* **105**, 042411 (2014).
  - [62] J. Lee, W. Falls, R. Oszwaldowski, and I. Žutić, *Appl. Phys. Lett.* **97**, 041116 (2010).
  - [63] O. Lopes Sanchez, E. Alacro Llado, V. Koman, A. Fontcuberta i Morral, A. Radenovic, and A. Kis, *ACS Nano* **8**, 3042 (2014).

## DEVICE FABRICATION

The dual-gated monolayer WSe<sub>2</sub> (MoSe<sub>2</sub>) field-effect transistors (FETs) were fabricated by the dry transfer technique. As shown in Fig. 5, hexagonal boron nitride (h-BN) of  $\sim 20$  nm thickness serves as top and back gate dielectric. Few-layer graphene is used for both top and back gate electrodes. Few-layer graphene is also used for source and drain contacts to monolayer WSe<sub>2</sub> (MoSe<sub>2</sub>). Atomically thin flakes of h-BN, graphene, and WSe<sub>2</sub> (MoSe<sub>2</sub>) were first mechanically exfoliated from bulk crystals onto silicon substrates covered with a 280-nm layer of thermal oxide. Their thickness was first estimated from their optical contrast and then confirmed by atomic force microscopy (AFM) or photoluminescence (PL) spectroscopy. The chosen flakes were then picked up layer by layer with a stamp made of a thin layer of polypropylene carbonate (PPC) on polydimethylsiloxane (PDMS). Using a micromanipulator under a microscope, we were able to align the flakes with the accuracy of  $\sim 1$   $\mu\text{m}$ . The stack was then released onto a silicon substrate with pre-patterned gold electrodes to form the dual gate FETs. The PPC residue on the device was removed before the optical measurements by dissolving in anisole.

## REFLECTION CONTRAST SPECTROSCOPY

The reflection contrast measurement was performed in a close-cycle cryostat from 4 K to 300 K. Broadband radiation from a supercontinuum light source was focused by a 40x objective onto the sample to a spot diameter of  $\sim 1$   $\mu\text{m}$ . The reflected light was collected by the same objective and detected by a spectrometer equipped with a charge-coupled-device (CCD). The excitation power on the device was kept below 10  $\mu\text{W}$ . The reflection contrast spectrum  $(R' - R)/R$  was obtained by measuring the reflectance from the part of the device with and without monolayer WSe<sub>2</sub> (MoSe<sub>2</sub>)  $R'$  and  $R$ .

With the combination of the top and back gates, the doping density and the vertical electric field in monolayer WSe<sub>2</sub> (MoSe<sub>2</sub>) can be tuned independently. We focus on the doping density effects in this study. The vertical electric field was kept at 0 by applying the same voltage on both the top and back gate since the top and back h-BN dielectric layer have the same thickness. The doping density (including both the free and localized charge carriers) can be evaluated by

$$n = \frac{\varepsilon \varepsilon_0}{t} V, \quad (12)$$

where  $\varepsilon_0$  is the vacuum permittivity,  $\varepsilon$  is the relative dielectric constant of h-BN ( $\sim 2.7$ ),  $t$  is the thickness of the h-BN layer, and  $V$  is the combined top and back gate voltage. For the devices shown in Fig. 1 of the main text, 1 V is equivalent to a doping density of  $7.5 \times 10^{11} \text{ cm}^{-2}$ .

## BARE COULOMB POTENTIAL AND GEOMETRIC CORRECTIONS

The bare Coulomb potential, that is, the potential unscreened by free charge carriers, can be obtained from the

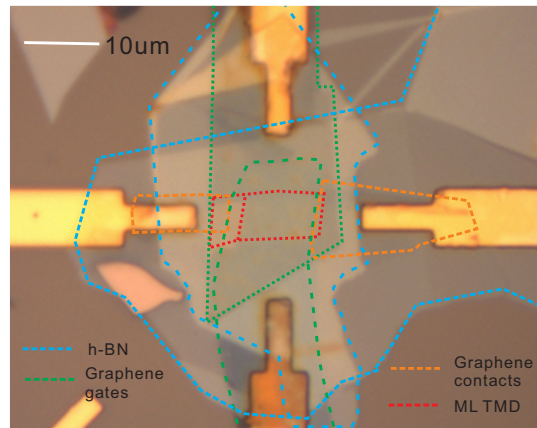


FIG. 5. (Color online) Optical microscope image of a dual-gate device of WSe<sub>2</sub>. The boundary of each component is shown in dashed lines. The scale bar is 10  $\mu\text{m}$ .

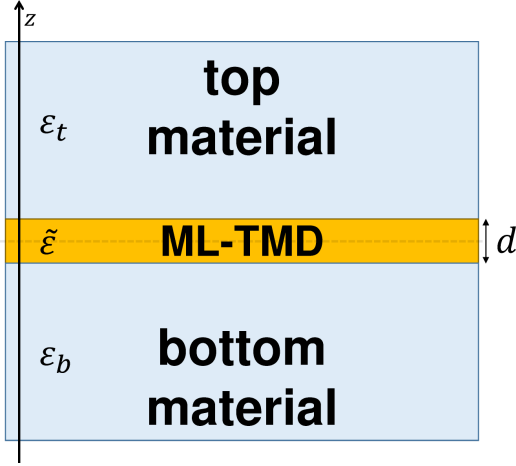


FIG. 6. (Color online) Geometry of the setup: A transition-metal dichalcogenide (TMD) monolayer of thickness  $d$  and dielectric constant  $\tilde{\epsilon}$  is embedded in two other materials with dielectric constants  $\epsilon_t$  and  $\epsilon_b$ .

Poisson equation, which in cylindrical coordinates  $(\rho, z)$

reads as

$$\nabla [\kappa(z) \nabla \phi(\boldsymbol{\rho} - \boldsymbol{\rho}'; z, z')] = 4\pi e \delta(\boldsymbol{\rho} - \boldsymbol{\rho}') \delta(z - z') \quad (13)$$

for a point charge located in a geometry as shown in Fig. 6. Here, the relative dielectric constant is given by

$$\kappa(z) = \begin{cases} \epsilon_t & \text{for } z > d/2 \\ \tilde{\epsilon} & \text{for } -d/2 < z < d/2 \\ \epsilon_b & \text{for } z < -d/2. \end{cases} \quad (14)$$

Introducing the Fourier transform of  $\phi$  with respect to the in-plane coordinates  $\boldsymbol{\rho}$  and insertion in Eq. (13) yields

$$\frac{d}{dz} \left[ \kappa(z) \frac{d\phi(\mathbf{q}; z, z')}{dz} \right] - \kappa(z) q^2 \phi(\mathbf{q}; z, z') = 4\pi e \delta(z - z'). \quad (15)$$

This equation is then solved for  $z = z' = 0$ , where we require the global solution to be continuous and its derivative to be piecewise continuous with a jump of  $4\pi e$  at  $z = z'$ .

After we have determined the potential  $\phi(\mathbf{q}; 0, 0)$  in this way, the bare Coulomb interaction between two electrons in the  $xy$ -plane ( $z = z' = 0$ ) can be calculated as

$$v_{\mathbf{q}} = -e\phi(\mathbf{q}; 0, 0) = \frac{2\pi e^2}{q} \frac{(\tilde{\epsilon}^2 - \epsilon_t \epsilon_b) + (\tilde{\epsilon}^2 + \epsilon_t \epsilon_b) \cosh(qd) + \tilde{\epsilon}(\epsilon_t + \epsilon_b) \sinh(qd)}{\tilde{\epsilon}[(\tilde{\epsilon}^2 + \epsilon_t \epsilon_b) \sinh(qd) + \tilde{\epsilon}(\epsilon_t + \epsilon_b) \cosh(qd)]}. \quad (16)$$

For thin layers  $qd \ll 1$ ,  $1/v_{\mathbf{q}}$  can be expanded in powers of  $qd$ , which yields

$$\begin{aligned} v_{\mathbf{q}} &\approx \frac{2\pi e^2}{q} \frac{1}{\frac{\epsilon_t + \epsilon_b}{2} + \frac{\tilde{\epsilon}d}{2} \left(1 - \frac{\epsilon_t^2 + \epsilon_b^2}{2\tilde{\epsilon}^2}\right)} \\ &= \frac{2\pi e^2}{\epsilon q + r_0 q^2}, \end{aligned} \quad (17)$$

where

$$\epsilon = \frac{\epsilon_t + \epsilon_b}{2} \quad (18)$$

is the average dielectric constant from the bottom and top materials surrounding the monolayer, and

$$r_0 = \frac{\tilde{\epsilon}d}{2} \left(1 - \frac{\epsilon_t^2 + \epsilon_b^2}{2\tilde{\epsilon}^2}\right) \quad (19)$$

can be interpreted as the polarizability of the monolayer. Our results are consistent with those obtained in Ref. [26]. In the limit of  $\epsilon_t/\epsilon_b \ll \tilde{\epsilon}$ ,  $r_0 = \tilde{\epsilon}d/2$  and we recover the result derived in Refs. [51, 52].

The interaction given by Eqs. (17)-(19) has proven to be highly successful in capturing the excitonic properties of ML-TMDs [19]. Using  $\epsilon_t = \epsilon_b = 2.7$  for h-BN,  $\tilde{\epsilon} = 9.05$  for MoSe<sub>2</sub>,  $\tilde{\epsilon} = 7.25$  for WSe<sub>2</sub>, and estimating  $d \approx 1$  nm,

Eqs. (18) and (19) yield  $\epsilon = 2.7$  as well as  $r_0 = 4.1$  nm for MoSe<sub>2</sub> and  $r_0 = 3.1$  nm for WSe<sub>2</sub>. Typically, in order to achieve better agreement with experiment,  $r_0$  has to be increased further from this estimate [25]. However, since the focus of our work is on the energy shift due to many-body interactions, which is not qualitatively affected by  $r_0$ , we use the aforementioned estimates  $r_0 = 4.1$  nm for MoSe<sub>2</sub> and  $r_0 = 3.1$  nm for WSe<sub>2</sub>.

The interaction in (17) is used to calculate the screened interaction  $W(\mathbf{q})$  using the random-phase approximation. The choice of the random-phase approximation over the Thomas-Fermi one is especially relevant in TMDs, where excitons remain bound across wide ranges of temperature and free-charge densities compared with typical semiconductor quantum wells [24, 45].

## DISORDER PARAMETER

To include disorder on a phenomenological level, we follow the procedure from Ref. 38 as detailed in the main text, and we obtain good agreement with the experimental data by choosing  $s = 5$  meV. For illustration, Fig. 7 shows the peak position of the 1s exciton in MoSe<sub>2</sub> and WSe<sub>2</sub> for various disorder parameters as a function of the charge density  $n$ . If no disorder is taken into account

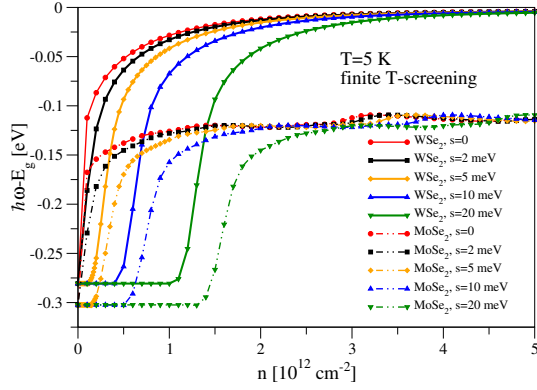


FIG. 7. (Color online) Calculated density dependence of the peak position of the 1s exciton for MoSe<sub>2</sub> and WSe<sub>2</sub> and different disorder parameters  $s$ .

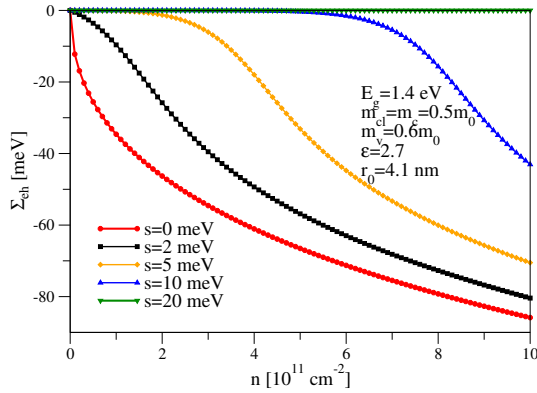


FIG. 8. (Color online) Calculated density dependence of the bandgap renormalization for MoSe<sub>2</sub> used in Fig. 7 above for densities up to  $n = 10^{12} \text{ cm}^{-2}$ .

( $s = 0$ ), the binding energy decreases quickly with doping, whereas large values of  $s$  result in a weak doping dependence for  $n$  up to several  $10^{11} \text{ cm}^{-2}$ .

The energy position of  $X^0$  is affected by the gate-induced charge density  $n$  via two competing effects: A blueshift originating from a reduced binding energy due to the screening of the Coulomb attraction and a redshift originating from the bandgap renormalization due to exchange and correlation. Whereas this gate-induced bandgap renormalization  $\Sigma_{\text{eh}}$  is negligible in ML-WX<sub>2</sub>,  $\Sigma_{\text{eh}} \sim 0$ ,  $\Sigma_{\text{eh}}$  can be of the order of several tens of meV in ML-MoX<sub>2</sub>. This difference between the two compounds arises because only the lower spin-split valleys are populated for low densities. The gate-induced bandgap renormalization  $\Sigma_{\text{eh}}$  is described (within the

plasmon-pole approximation) by Eqs. (9) and (10) in the main text. For the parameters used in Fig. 7 above, we show  $\Sigma_{\text{eh}}$  as a function of the density  $n$  in Fig. 8 above. This energy redshift of the bandgap then counteracts the blueshift due to reduced binding energy.

## COMPUTATIONAL DETAILS

If we do not take into account intervalley coupling (as is done in this work), the excitons can be calculated for each valley and spin-degree-of-freedom separately. Then, the problem reduces to Eq. (1) in the main text with only one conduction and one valence band. In order to diagonalize Eq. (1) in the main text, we use a coarse uniform  $N \times N$   $k$ -grid with a spacing of  $\Delta k = 2\pi/(Na_0)$  and  $a_0 = 3.29 \text{ \AA}$  in each direction as well as an upper energy cutoff  $E_{\text{cu}}$ . The Coulomb matrix elements  $W(\mathbf{k} - \mathbf{k}')$ , however, are not evaluated at the grid points of the  $N \times N$   $k$ -grid, but instead are averaged over a square centered around the coarse grid point  $\mathbf{k} - \mathbf{k}'$  with side widths  $\Delta k$  on a fine  $N_{\text{int}} \times N_{\text{int}}$  grid [with a corresponding spacing of  $\Delta k_{\text{int}} = \Delta k/N_{\text{int}} = 2\pi/(NN_{\text{int}}a_0)$ ]. For our numerical calculations, we have used  $N = N_{\text{int}} = 100$  and an energy cutoff 1.2 eV above the band gap,  $E_{\text{cu}} = E_g + 1.2 \text{ eV}$ . This procedure ensures that our numerical calculations converge reasonably fast and we find that the 1s binding energy changes by less than 0.5% when going from  $N = 100$  to  $N = 200$ .

## BROADENING FOR THE ABSORPTION CALCULATION

Having solved Eq. (1) in the main text, we use its eigenstates and eigenvalues to calculate the optical absorption via Eq. (11) in the main text. Equation (11) contains a Lorentzian function

$$\mathcal{L}(\hbar\omega; \Omega_S, \Gamma) = \frac{1}{\pi} \frac{\Gamma}{(\hbar\omega - \Omega_S)^2 + \Gamma^2} \quad (20)$$

to account for homogenous broadening due to electron-electron and electron-lattice interactions. This broadening is modeled by [58, 59]

$$\Gamma = \Gamma_0 + \Gamma_n \left[ 1 - e^{-\frac{n}{n_0}} \right] + \Gamma_T \left[ 1 - e^{-\frac{T}{T_0}} \right], \quad (21)$$

where we use typical values  $\Gamma_0 = 2 \text{ meV}$ ,  $\Gamma_n = 8 \text{ meV}$ ,  $\Gamma_T = 10 \text{ meV}$ ,  $n_0 = 3 \times 10^{11} \text{ cm}^{-2}$ , and  $T_0 = 300 \text{ K}$  [49].